ADVANCED MATERIALS
www.advmat.de

Performance Limits of an Alternating Current Electroluminescent Device

*Vivian Wang, Yingbo Zhao, and Ali Javey**

The use of an alternating current (AC) voltage is a simple, versatile method of producing electroluminescence from generic emissive materials without the need for contact engineering. Recently, it was shown that AC-driven, capacitive electroluminescent devices with carbon nanotube network contacts can be used to generate and study electroluminescence from a variety of molecular materials emitting in the infrared-to-ultraviolet range. Here, performance trade-offs in these devices are studied through comprehensive device simulations and illustrative experiments, enhancing understanding of the mechanism and capability of electroluminescent devices based on alternating as opposed to direct current (DC) schemes. AC-driven electroluminescent devices can overcome several limitations of conventional DC-driven electroluminescent devices, including the requirement for proper alignment of material energy levels and the need to process emitting materials into uniform thin films. By simultaneously optimizing device geometry, driving parameters, and material characteristics, the performance of these devices can be tuned. Importantly, the turn-on voltage of AC-driven electroluminescent devices approaches the bandgap of the emitting material as the gate oxide thickness is scaled, and internally efficient electroluminescence can be achieved using low-mobility single-layer emitter films with varying thicknesses and energy barrier heights relative to the contact.

Common light-emitting devices rely on the phenomenon of electroluminescence (EL), the emission of light in response to electrical excitation. These devices include the light-emitting diode (LED), a two-terminal device driven by a direct current (DC) voltage source. Bright and efficient LEDs have already been successfully developed to generate light emission from a wide variety of materials, from inorganic III–V semiconductors[1,2] to colloidal quantum dots (QDs)[3,4] to organic molecules.[5] Generally, electrons and holes are simultaneously injected into an emissive material from n- and p-type contacts, migrate across the emitting layer, and recombine to produce light. This process can occur with nearly perfect internal quantum efficiency (IQE).[6] It is also possible to generate electroluminescence by employing an alternating current (AC)-driving scheme.[7] Early examples include ZnS-phosphor-based devices,[8] which rely on extremely high operating voltages to achieve impact excitation to excite luminescent centers. Other examples include double-insulator devices where both electrodes are covered by a dielectric layer, and carriers are solely generated from internal charge generation layers.[9]

Conversely, both charge carriers can be injected directly from contacts. In vertically structured field-induced polymer electroluminescent devices, charge carriers are injected from an electrode and/or generated in charge generation layers.[10–12] EL has also been demonstrated with a laterally structured capacitive device structure in which materials are deposited on top of a gate oxide layer across which AC voltage is applied.[13–15] A more complex transistor-based structure that applies an additional drain–source bias can also be adopted to generate light from various materials.[16,17] These examples, which use microscale metal contacts to inject carriers, may be sufficient to produce AC EL from materials with relatively high mobility; however, denser electrical contacts are preferable for generating bright AC EL from other kinds of materials, including molecular emitters with poor mobility.[18,19] To this end, self-assembled carbon nanotube (CNT) networks[20] can be used as a porous top contact to increase contact density and emission intensity.[21] Due to the lateral nature of charge injection, the emitting material does not need to be suited for further processing, and optical properties can be easily probed without requiring transparent contacts, unlike vertical multilayered devices in which the emitting layer is sandwiched between multiple films.

In this work, we study the performance limits of a generic AC electroluminescent device in which direct bipolar charge injection is achieved with a single CNT network electrode, using numerical device simulations to corroborate and understand experimental measurements. We previously demonstrated such a device for applications in electroluminescence spectroscopy and sensing,[21] but more elaborate knowledge is required to understand the scope of compatible materials as well as the operating parameters that are optimal for different

V. Wang, Dr. Y. Zhao, Prof. A. Javey
Electrical Engineering and Computer Sciences
University of California at Berkeley
Berkeley, CA 94720, USA
E-mail: ajavey@berkeley.edu
V. Wang, Dr. Y. Zhao, Prof. A. Javey
Materials Sciences Division
Lawrence Berkeley National Laboratory
Berkeley, CA 94720, USA

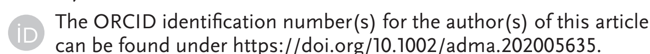
The ORCID identification number(s) for the author(s) of this article can be found under https://doi.org/10.1002/adma.202005635.

DOI: 10.1002/adma.202005635

 © 2020 Wiley-VCH GmbH

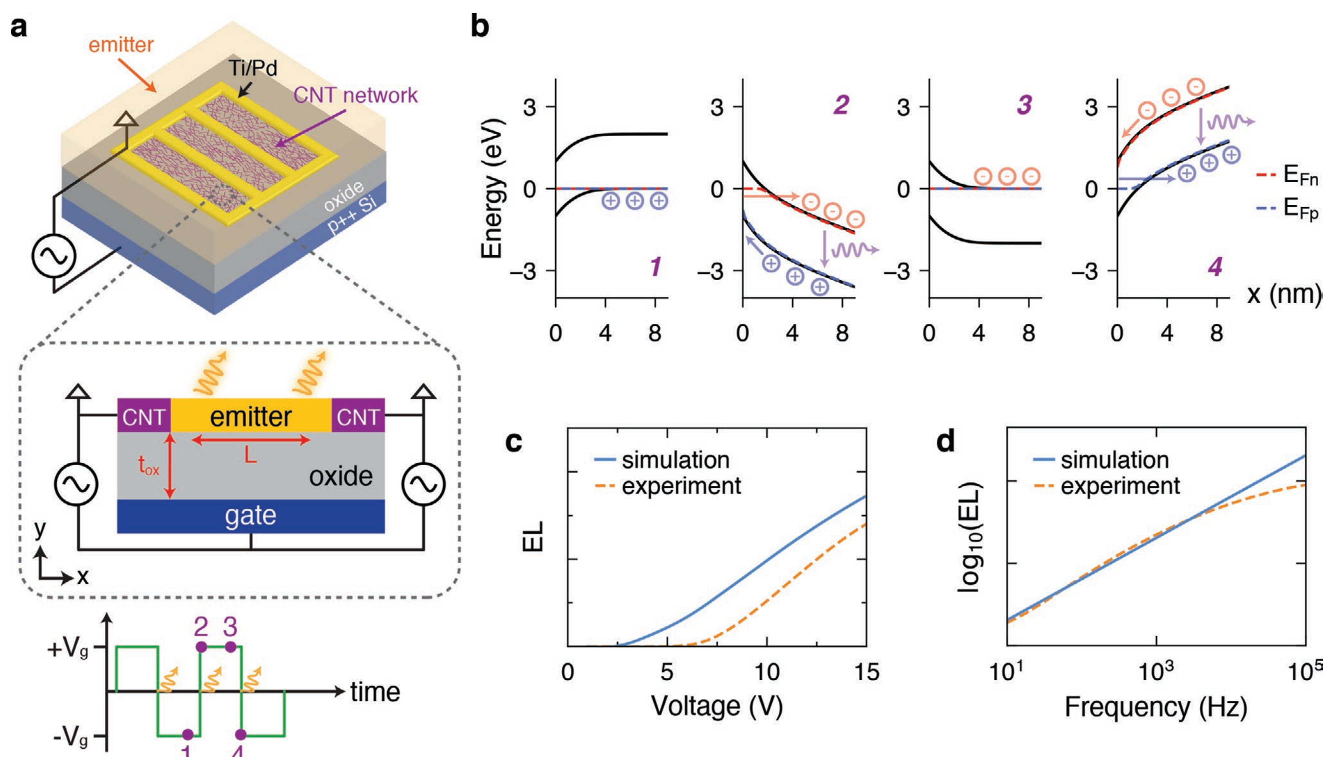

Figure 1. a) Schematic of an AC electroluminescent device with a metal grid electrode (yellow) contacting a CNT network (purple lines) on an oxide substrate (gray). Square wave AC voltage is applied between the p++ Si gate (blue) and the grounded metal electrode. To capture device behavior, we simulate the region between two individual CNT contacts. b) Energy band diagrams at the CNT–emitter interface at the square wave timepoints indicated in (a). Quasi-Fermi levels for electrons and holes are shown in red and blue, respectively. c) EL intensity as a function of gate voltage from simulation (blue) and experiment (orange). d) EL intensity as a function of square wave frequency from simulation and experiment. Experimental data were measured from devices with red CdSSe/ZnS quantum dots on 50 nm SiO_2 gate oxide using a 100 kHz, 10 V square wave.

material samples. Through studies of device scaling, we show that turn-on characteristics of the AC electroluminescent device are controlled by vertical scaling of the device's dimensions. We further elucidate the interplay between charge transport, brightness, and efficiency by analyzing spatial and temporal variations of charge density and carrier recombination. Finally, we investigate how device design affects fundamental efficiency losses and transient responses, informing directions of future improvement for AC electroluminescent devices and demonstrating that efficient light emission can be achieved with AC voltages depending on the material and device parameters.

The structure and operating scheme of the AC light-emitting device under study is schematically illustrated in **Figure 1**a. The device consists of a layer of emissive semiconducting material deposited on top of an oxide layer. AC voltage is applied across a bottom gate contact and top CNT network source contact. Experimentally, we fabricated this device structure on a 50 nm SiO_2/p++ Si substrate in which the p++ Si substrate serves as the bottom gate contact and a metal grid is used to contact the CNT network for probing. When a pulsed gate voltage with a finite slew rate is applied across the gate and source contacts, light emission is observed after voltage transitions as confirmed by earlier time-resolved EL measurements.[13] The proposed mechanism behind such a driving scheme has been discussed previously.[21] To briefly recapitulate, electrons accumulate in the emitter layer when the gate voltage is positive, causing there to be a large electron concentration but low hole concentration. When the gate voltage switches from positive to negative, the field across the device cannot change immediately, so the applied gate voltage instead drops across resistive components such as the emitter material. The large potential drop at the source contact–emitter interface results in steep band bending that enables carrier tunneling (Figure 1b). Holes are injected into the emitter layer as electrons either exit the semiconductor through the contact or recombine with holes. Eventually, the transient carrier action subsides and the band diagram resembles that of a metal-oxide-semiconductor capacitor at steady state until the subsequent negative to positive voltage transition, where a similar tunneling process occurs.

To further understand the operating characteristics and performance limits of such a device, we performed numerical simulations of the device using Sentaurus technology computer-aided design (TCAD) tools, which simultaneously solve the Poisson and carrier continuity equations with a drift-diffusion model involving Fermi statistics and radiative carrier recombination.[22,23] We assume equal and constant electron and hole mobilities as well as ambipolar contacts for symmetry. In both simulation and experiment, a certain turn-on voltage is required to observe EL, after which point the EL intensity increases approximately linearly with the amplitude of the square wave gate voltage (Figure 1c). EL occurs immediately following each voltage transition and lies dominantly near the source contacts

© 2020 Wiley-VCH GmbH

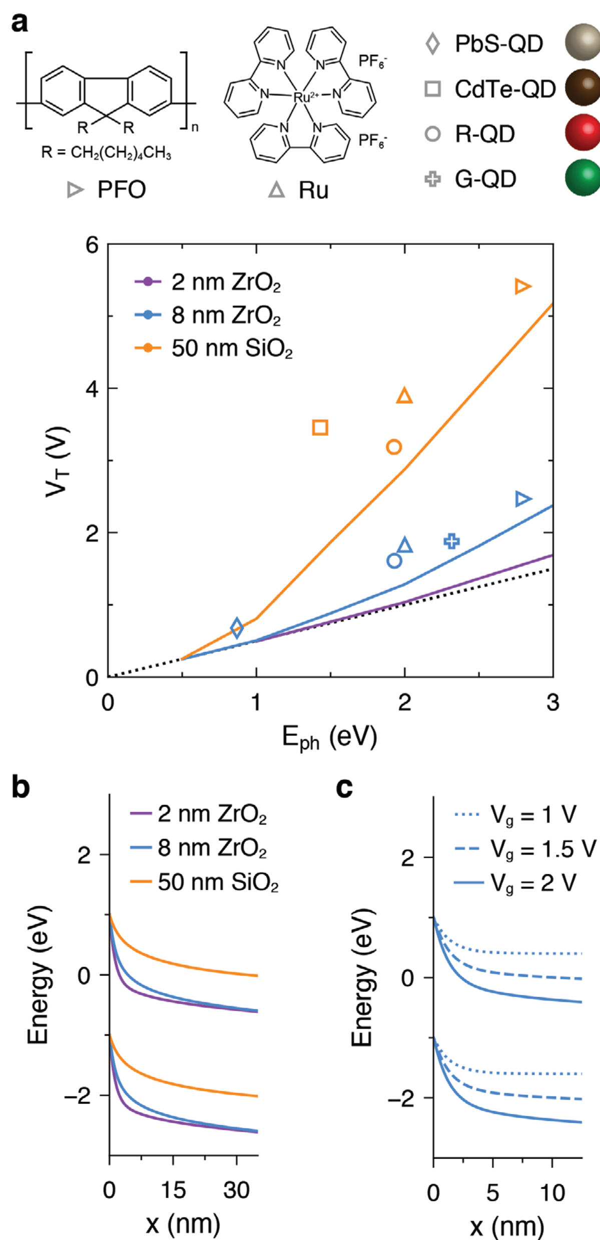

Figure 2. a) Turn-on voltage as a function of photon energy from simulation (solid lines) and experiment (open markers). Simulations were performed in 0.5 eV bandgap energy increments for devices with gate oxide thicknesses roughly corresponding to the fabricated devices indicated in the legend (2 nm $ZrO_2 \approx 0.4$ nm EOT, 8 nm $ZrO_2 \approx 1.4$ nm EOT, and 50 nm $SiO_2 = 50$ nm EOT). The black dotted line represents the curve $V_T = E_{ph}/2$. Experimental data were measured using a 100 kHz square wave. Abbreviations: PbS-QD (PbS quantum dot), CdTe-QD (CdSeTe/ZnS quantum dot), R-QD (630 nm red CdSSe/ZnS quantum dot), Ru ($Ru(bpy)_3(PF_6)_2$), G-QD (520 nm green CdSSe/ZnS quantum dot), PFO (poly(9,9-dioctylfluorene)). b) Energy band diagrams at a source contact for devices with different gate dielectrics at $V_g = 2$ V. c) Energy band diagrams at a source contact for a device with 2 nm ZrO_2 and different applied gate voltages. The simulated emitter layer bandgap is $E_g = 2$ eV.

in most cases, so the EL intensity should scale linearly with the number of voltage transitions or square wave frequency. Experimentally, the EL intensity does scale linearly with square wave frequency up to a certain cut-off frequency, after which the EL intensity rolls off since the device can no longer reach steady-state conditions during square wave pulses (Figure 1d). Based on this model, we studied trends between material properties (e.g., carrier mobility and bandgap), device structure (e.g., CNT network density, oxide, and emitter layer thickness), and performance characteristics (e.g., turn-on voltage, brightness, and quantum and power efficiency).

While various AC electroluminescent devices have been proposed and demonstrated in the past, these devices largely rely on high operating voltages (in the tens to hundreds of volts) to achieve reasonable electroluminescence, rendering them less practically appealing than their DC counterparts.[12,24,25] In our device, the turn-on voltage reflects the presence of a charge injection barrier at the source–semiconductor contact as well as any external parasitic components in the experimental measurement. We performed EL simulations at different peak-to-peak gate voltages for devices with varying oxide thicknesses (Figure S1, Supporting Information) in order to understand global trends in turn-on voltage scaling. As the bandgap of the emissive material increases, the threshold voltage increases superlinearly compared to the theoretical limit ($V_T \approx \pm E_g/2$), meaning that it is harder to achieve low turn-on voltage for materials with large bandgaps as a result of the increased injection barrier.

Due to the unique ability of our device to generate EL from emissive materials with nearly any bandgap in the infrared-to-ultraviolet range, we can study fundamental scaling relationships of turn-on voltage versus emitter bandgap using a single device, without any need to design different electron and hole contacts for different materials. Experimental EL data from devices with different gate oxide thicknesses agree well with the simulated model (**Figure 2**a). In particular, scaling down the oxide thickness reduces the turn-on voltage. As in conventional field-effect transistors, gate control of the emissive semiconducting material depends on the equivalent oxide thickness (EOT) of the gate oxide, which is defined as $t_{ox}(\varepsilon_{SiO_2}/\varepsilon_{ox})$ for a gate oxide of thickness t_{ox} and relative dielectric constant ε_{ox}.[26] The EOT can be reduced by decreasing the oxide thickness or increasing the dielectric constant of the oxide layer. The charge on a capacitor at steady state depends on the gate capacitance and voltage ($Q \propto C_{ox}(V_g - V_T)$); increasing the capacitance decreases the operating voltage required for equivalent charge input. It is worth noting that high-κ dielectrics have been previously applied to reduce the turn-on voltage in AC electroluminescent devices with double dielectric layers, albeit based on a different mechanism which relies on field-dependent charge regeneration due to the absence of direct carrier injection.[27] For materials with very low bandgap, the EOT has little effect on the turn-on voltage, which remains near the bandgap for all oxide thicknesses shown. The turn-on voltage approaches the theoretical limit across a larger range of emitter bandgaps as the EOT is decreased, as exemplified by simulations of a device with a 2 nm high-κ ($\varepsilon_{ox} \approx 22$) oxide layer with EOT ≈ 0.4 nm.

Energy band diagrams at the source–semiconductor interface shed light on the physical mechanism underlying the reduction in turn-on voltage. As the EOT decreases and gate capacitance increases, the electric field or steepness of band bending at the source contact during voltage transitions increases, thereby thinning the tunneling barrier for carrier injection at a fixed

© 2020 Wiley-VCH GmbH

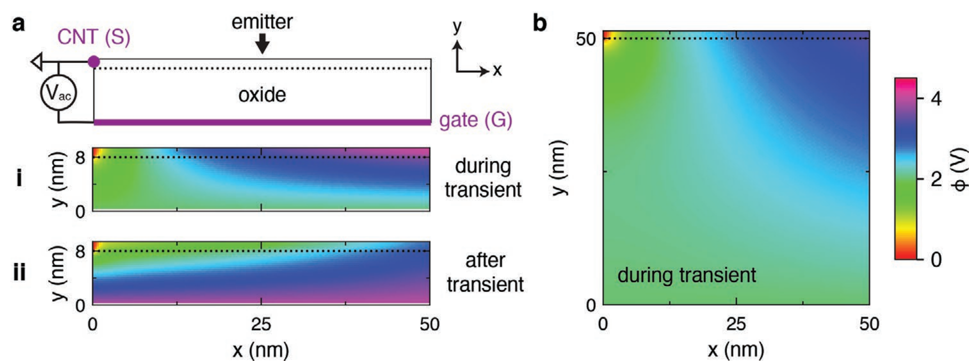

Figure 3. a) Schematic of the simulated device with a grounded CNT source contact on the top left at $x = 0$ and a gate electrode on the bottom at $y = 0$; i,ii) the 2D electric potential distributions near the source contact during and after a square wave voltage transition, respectively. The simulated device has an 8 nm thick high-κ gate dielectric (EOT ≈ 1.4 nm). b) 2D electric potential distribution during a square wave voltage transition for a device with a 50 nm thick SiO_2 gate dielectric. The applied gate voltage is ±4 V and the emitter layer mobility is $\mu = 10^{-3}$ cm^2 V^{-1} s^{-1}.

gate voltage (Figure 2b). Increasing the applied gate voltage has a similar effect (Figure 2c). Since the breakdown voltage of the gate oxide scales with oxide thickness, practical choices for the oxide thickness should consider both the viable operating voltage regime and the achievable turn-on voltage. Altogether our results show that the turn-on voltage corresponds to the transition from injection- to transport-limited behavior and depends on both the emitter bandgap and gate oxide thickness. Other parameters, such as carrier mobility in the emitter layer, have less effect on the turn-on voltage (Figure S2, Supporting Information).

2D plots of the electrostatic potential show the evolution of voltage drops present in the device. During the gate voltage transient, the charge on the capacitor cannot switch polarity immediately, thus causing the electric potential to drop at the contact–emitter interface first. This regime, in which the potential changes mostly along the lateral (x) direction, is depicted in **Figure 3**a-i. As time elapses, the potential drops increasingly across the oxide as opposed to across the emitter layer, yielding greater changes in electrostatic potential in the vertical (y) direction across the oxide (Figure 3a-ii). When the oxide is thick and of low dielectric constant, less voltage is dropped near the CNT contact, which reflects the more gradual band bending and decreased level of carrier injection (Figure 3b). In this case, the gate capacitance is smaller, and less charge is accumulated in the emitter layer during the steady-state periods of the square wave pulse.

In general, the turn-on voltage of AC electroluminescent devices with ambipolar contacts should approach the optical energy gap of the emitting material as the EOT is decreased. The simulated turn-on voltages for charge injection and EL consistently underestimate the experimentally measured threshold voltages, in part due to exclusion of excitonic effects in the simulation model. In excitonic materials, electrons and holes undergo recombination by first forming bound pairs (excitons) with energies slightly smaller than the bandgap for free carriers. The difference between the measured photon energy and the bandgap for transport depends on the excitonic binding energy. Furthermore, it is unlikely that the CNT contacts are perfectly ambipolar with respect to the experimentally measured materials. When the source contacts have p- or n-type work functions, the turn-on voltage increases by an amount similar to the increase in Schottky barrier height for the harder-to-inject carrier (Figure S3, Supporting Information). In this case, DC offsets can be applied to the AC gate voltage to offset detrimental work function differences and restore low-voltage device behavior equivalent to the case of midgap contacts. For example, it is more difficult to inject holes into the emitter material using n-type contacts because of the increased Schottky barrier height. Applying a negative DC offset pulls the emitter bands upward, yielding sharper band bending that thins the barrier and enables carrier tunneling (Figure S3, Supporting Information). Importantly, the EL at moderate-to-high voltage does not depend greatly on the Schottky barrier height or work function difference between the source contact and energy levels of the emissive material. As a result, the conventional requirement for Ohmic contacts[28] or low injection barriers can be overcome.

Once charge injection into the emissive material has been achieved, charge carriers move through the emitter layer and a fraction eventually undergoes radiative recombination to emit photons. Although large strides have been made toward improving the mobilities of molecular emissive materials such as those used in organic LEDs (OLEDs), these materials largely possess limited carrier mobilities (<1 cm^2 V^{-1} s^{-1}) that are orders below those of common inorganic semiconductors.[19,29,30] It is even more difficult to design molecular systems with both high carrier mobility and efficient solid state emission for optoelectronic applications, particularly in the case of solution-processable emitters.[31–33] In light of these constraints, it is useful to study the necessity of maintaining high carrier mobility in electroluminescent devices. Unlike traditional vertically stacked LED architectures, our AC electroluminescent device relies on lateral transport from single contacts that inject both electrons and holes. As carrier mobility in the emissive layer decreases, the total amount of radiative recombination between an individual pair of CNT contacts increases (**Figure 4**c). For very low carrier mobilities, the amount of EL saturates or slightly diminishes depending on the spacing between the contacts. The recombination efficiency increases concomitantly with decreasing carrier mobility until a saturation value of around 90% (Figure 4d). The recombination efficiency is calculated as the ratio of radiative recombination events to the number of injected electron–hole pairs; 100% recombination efficiency

© 2020 Wiley-VCH GmbH

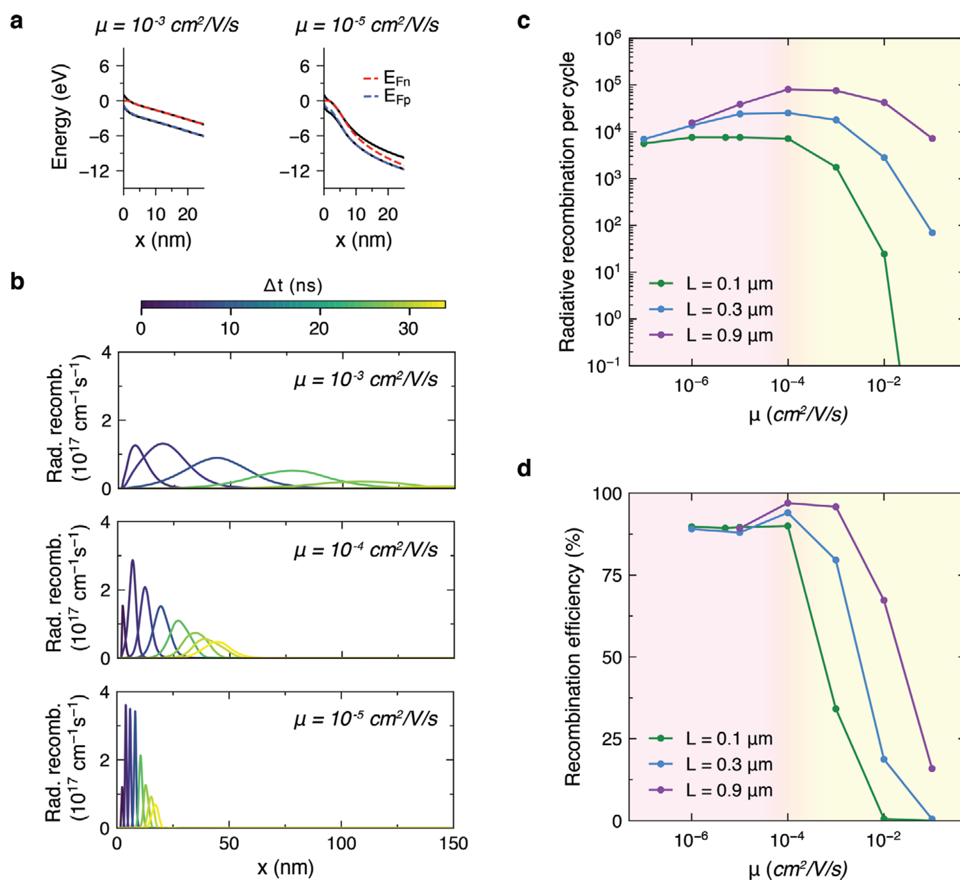

Figure 4. a) Energy band diagrams at a source contact for devices with an emitter layer carrier mobility of 10^{-3} cm^2 V^{-1} s^{-1} (left) or 10^{-5} cm^2 V^{-1} s^{-1} (right). b) Radiative recombination profiles over space (in the lateral direction along the length of the emitter layer) at different timepoints Δt after the start of a voltage transition. c) Total radiative recombination and d) recombination efficiency per cycle as a function of carrier mobility in the emitter layer for devices with different average CNT–CNT spacings L. Shorter L corresponds to denser CNT networks. Simulations were performed for devices with a 50 nm SiO_2 gate dielectric and ±12 V square wave gate voltage.

occurs when all electron–hole pairs produce a photon. Although we assume that the emissive material has unity quantum yield in the simulation (i.e., there are no nonradiative recombination pathways), the time-alternating injection of electrons and holes, as well as finite slew rate do not guarantee that all injected charge carriers undergo recombination with opposite charge carriers, and some of the carriers will instead return to the electrode during voltage transients.

The influence of charge transport can be explained by examining the calculated band diagrams. When carrier mobility is low, charge carriers are unable to transport far into the emissive material and accumulate near the source contact, causing the electric potential to vary dramatically near the contact (Figure 4a). Quasi-Fermi level splitting only occurs near the contact, in accordance with the lack of injected charge carriers far from the contact. When the mobility is high, quasi-Fermi level splitting extends along the entire lateral length of the emitter layer as carriers populate the entire volume of the emissive material. At the gate voltage transition, the potential gradient is distributed gradually along the entire length of the emitter (Figure S4a,b, Supporting Information). Radiative recombination, which requires the simultaneous presence of both electrons and holes, is localized entirely near the source contact when the mobility is low (Figure 4b), as confirmed by the fact that changes in steady-state carrier concentrations are only observed near the contact (Figure S4c,d, Supporting Information). The length of the emission region scales roughly with $\sqrt{\mu}$; tenfold increases in carrier mobility lead to approximately threefold increases in emission length, consistent with the scaling of diffusion length in semiconductors. In low-mobility materials, emission is limited to near the source contact in both the lateral and vertical directions, as shown by simulated 2D emission profiles for devices with thick emitter layers (Figure S5, Supporting Information). These results resemble those of OLEDs, in which the recombination zone is closer to the contact injecting the lower mobility carrier.[28,34] As the distance between CNT contacts increases, the EL intensity and recombination efficiency increase because longer emission lengths can be accommodated. Therefore, carrier mobility and CNT network density should be simultaneously optimized to yield transport lengths similar to the spacing of the CNT network. EL tends to increase, then saturate as the thickness of the emitter layer increases, suggesting that precise control of the emitter layer thickness is not essential for bright EL. At the same time, EL can be obtained from arbitrarily thin materials contacting the CNT network, including those with nonuniform

© 2020 Wiley-VCH GmbH

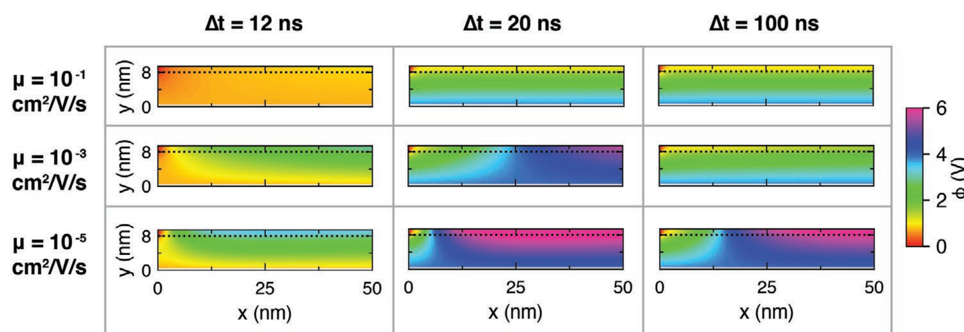

Figure 5. 2D maps of the electrostatic potential for devices with an 8 nm thick high-κ gate dielectric (EOT ≈ 1.4 nm). Simulations were performed with a ±4 V square wave gate voltage, and the plots represent behavior from the upward voltage transition (from –4 to +4 V). For each emitter layer mobility case (shown in separate rows), the potential map is plotted for different times Δt (shown in separate columns) after the start of the voltage transition at $t = 0$. The rise time of the voltage transition is 20 ns. From left to right, the columns correspond to the potential during the gate voltage transition, at the end of the gate voltage transition, and 80 ns after the end of the gate voltage transition. The black dotted line represents the interface between the gate oxide and the emitter layer as shown in Figure 3.

morphologies. This behavior contrasts that of conventional OLEDs, which show increased turn-on voltages and decreased luminance as the thickness of the emissive layer increases due to poor charge transport properties of molecular emitting materials.[35] Furthermore, the emissive materials in OLEDs must be able to form smooth and pinhole-free thin films on the order of up to tens of nanometers.[19]

The effect of emitter material mobility is illustrated in **Figure 5** for thin gate oxide devices where ±4 V square wave gate voltages are applied with a transient slew time of 20 ns. For $\mu = 10^{-1}$ cm^2 V^{-1} s^{-1}, the switch in applied gate voltage from –4 V (at $\Delta t = 0$ ns, where Δt denotes the time since the start of the voltage transition) to 4 V (at $\Delta t = 20$ ns) occurs nearly instantaneously across the oxide, with the electrostatic potential at the end of the voltage transition ($\Delta t = 20$ ns) varying linearly across the bulk of the oxide as expected for a capacitor under steady-state DC voltage. At $\Delta t = 12$ ns (the moment at which 60% of the voltage transition has elapsed), the gate contact voltage is +0.8 V and the potential near the contact is nearly uniformly equilibrated at this value. When the carrier mobility is reduced to 10^{-3} cm^2 V^{-1} s^{-1}, the steady-state electrostatic potential profile is observed somewhat later at $\Delta t = 100$ ns after the start of the voltage transition. When the carrier mobility is reduced even further to 10^{-5} cm^2 V^{-1} s^{-1}, the potential distribution does not reach the steady-state condition by $\Delta t = 100$ ns as large lateral potential drops have not yet subsided. Immediately after the voltage transition, dramatic lateral voltage drops are observed in the vicinity of the contact due to the low conductivity or large resistance of the emissive material in series with the oxide. Similar results are obtained for devices with thicker gate oxide (Figure S6, Supporting Information). To summarize, the temporal dynamics show that higher peak EL is in fact obtained in materials with lower carrier mobility as a result of spatial localization of the charge carriers and inability of the electric potential to drop across the oxide rapidly.

Surprisingly, a square wave gate voltage waveform with a fast slew rate is not necessary for bright EL when the charge carrier mobility is low. Experimentally, applying a sine wave gate voltage waveform yields similar EL levels as applying a square wave gate voltage waveform (Figure S7, Supporting Information), with EL only reduced by around 50% or less. The EL per cycle typically increases with sine wave frequency, as confirmed in simulation. Through numerical simulation, we find that the difference in EL when using a sine versus square wave gate voltage is smaller when the mobility is lower. Calculated energy band diagrams indicate that sufficiently steep band bending occurs at the contact following a switch in voltage polarity for either a sine wave or square wave, with quasi-Fermi level splitting being about equal to the bandgap in both cases. The overall lateral voltage drop across the emitter is greater when a square wave is applied, but carrier injection is located near the contact in either case as indicated by the lack of quasi-Fermi level splitting in the middle of the domain. The exact relationship between frequency (for a sine wave) or slew rate (for a square wave) scaling and emission intensity would depend on the radiative recombination rate in practice.

Until now, the presented results have assumed equal mobilities for electrons and holes. It has been shown that balance of charge carrier mobilities improves OLED brightness and efficiency by reducing the fraction of one carrier type that travels across the device without recombining.[34] Due to the alternating injection of carriers in the AC EL scheme, recombination efficiency is dominated by the lower mobility carrier; high efficiency can be achieved as long as one of the carriers has sufficiently low mobility (Figure S8, Supporting Information). If the hole mobility is greater than the electron mobility, then holes exit the emitter layer much faster than electrons are able to enter the emitter layer at the downward voltage transition, leading to negligible EL. However, at the upward transition, holes are able to populate the bulk of the emitter layer much faster while electrons exit slowly, giving rise to substantial EL comparable to the case of equal and low carrier mobility (Figure S9, Supporting Information). Asymmetric EL at voltage transitions therefore results not only from nonambipolar contacts[13] but also from asymmetric charge transport. Even when the charge carrier mobilities are unbalanced, EL can still be obtained by using a single contact to inject both carriers near the contact.

Aside from turn-on voltage and brightness, other important figures of merit for light-emitting devices include quantum and power efficiency. The IQE of a light-emitting device is given by $\eta_{\text{int}} = \phi\gamma$ and the external quantum efficiency (EQE)

 © 2020 Wiley-VCH GmbH

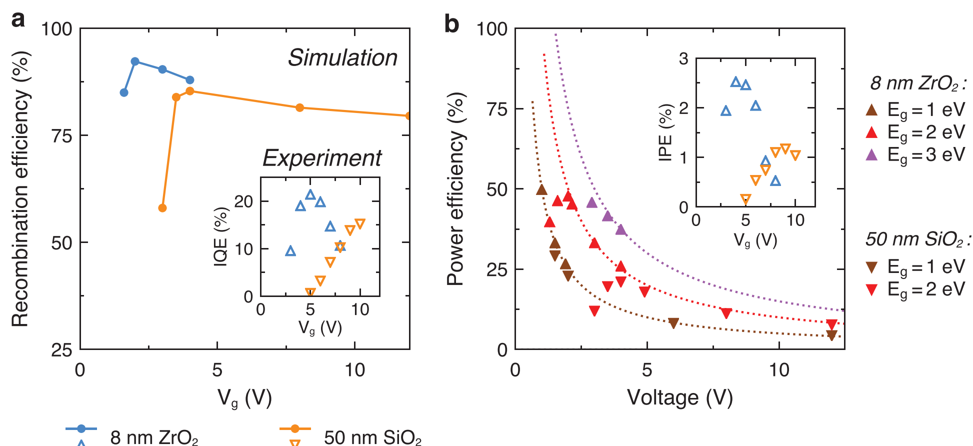

Figure 6. a) Gate voltage dependence of recombination efficiency from simulation (solid lines). The blue and orange data represent devices with 8 nm high-κ gate dielectric or 50 nm SiO_2 gate dielectric, respectively. Experimentally measured internal quantum efficiencies (IQE), which normalize for differences in light outcoupling, are shown in the inset (open markers). b) Gate voltage dependence of power efficiency from simulation for devices with different gate dielectric (upward triangles: 8 nm ZrO_2, downward triangles: 50 nm SiO_2) and emitter layer bandgap E_g. The dotted lines are guides to the eye and represent an inverse voltage relationship of the form E_g/V_g with a constant scaling factor. Experimentally measured internal power efficiencies (IPE) are displayed in the inset (colors same as in panel (a)). Data were measured from devices with a drop-cast $Ru(bpy)_3(PF_6)_2$ emitter layer ($E_g = 2$ eV).

is given by $\eta_{ext} = \eta_{int}\ \eta_{coupling}$, where ϕ relates to the intrinsic photoluminescence efficiency of the emissive material, γ is the recombination efficiency (fraction of injected charge carriers that recombine in the emissive layer; Figure S10 (Supporting Information)), and $\eta_{coupling}$ is the outcoupling efficiency (fraction of photons that are able to escape the device).[36] For organic excitonic materials with singlet emission, the intrinsic efficiency of the emissive material also takes r_{st}, the ratio of singlet to triplet excitons, into consideration. To evaluate the fundamental efficiency of an alternating-current-based carrier injection scheme, we focus on the efficiency of carrier injection leading to radiative recombination (γ), which is the term that depends on the mechanism of device operation. According to simulation, the recombination efficiency tends to increase with gate voltage near the turn-on voltage of the device, but slowly decreases thereafter (**Figure 6**a). The recombination efficiencies for devices with different oxide thicknesses are similar, with the thicker oxide device only being slightly less efficient. Peak recombination efficiency is achieved when the band bending is just steep enough to allow for efficient carrier tunneling and subsequent injection. Beyond this point, higher gate voltages increase the rate at which the steady-state carriers are swept out of the emissive material, decreasing the fraction of injected carriers that are able to recombine with opposite charge carriers exiting the emissive material.

Experimentally, we observe a similar trend for a high-κ gate oxide device with a drop-cast layer of $Ru(bpy)_3(PF_6)_2$ in which the IQE increases with voltage up to a certain point before decreasing (Figure 6a, inset). For simplicity, we performed the simulations assuming 100% quantum yield in the emitter layer; however, the experimentally measured materials have nonunity quantum yield.[37,38] Hence, the experimentally extracted internal quantum efficiencies, which are a product of ϕ and γ, do not reach the same levels as the calculated efficiencies, and, in this case, are around one-fifth lower than the simulated performance limit. This value is consistent with analogous photoluminescence quantum yield measurements of the drop-cast emitter layer on the device substrate. In addition, the peak experimental quantum efficiencies are achieved at almost double the gate voltage calculated from simulation, which may be a result of parasitic device resistances that reduce the voltage applied to the emitter as well as nonradiative recombination mechanisms that dampen the EL intensity at low carrier concentrations. As a qualitative example, the recombination efficiency increases monotonically with gate voltage up to $V_g = \pm 12$ V if we include trap-assisted Shockley–Read–Hall recombination in addition to radiative recombination in our simulated model (Figure S11, Supporting Information). Strikingly, the total amount of radiative recombination and net recombination efficiency does not depend on the contact work function or Schottky barrier height after the turn-on regime has been surpassed (Figure S12, Supporting Information), although unbalanced charge injection has been found detrimental to the performance of quantum dot LEDs[4] and OLEDs.[39] While devices simulated with p- and n-type contacts (0.1 eV Schottky barrier height in each case) show similar overall results as a device simulated with ambipolar contacts, EL at the upward voltage transition is higher with an n-type contact than with a p-type contact due to more facile electron injection, and vice versa at the downward transition.

Similar to our findings on recombination efficiency, larger CNT–CNT distances (corresponding to sparser CNT networks) are preferable for achieving higher power efficiency, particularly in materials with higher mobility (Figure S13, Supporting Information). Here power efficiency is defined as the time-averaged output light power (assuming photons are emitted with an energy equal to the bandgap) divided by the input electrical power, which is calculated by integrating the product of the time-dependent current and voltage over a full AC cycle. Power efficiency approximately depends on the quantum efficiency and the factor $(h\nu)/(qV)$ where $h\nu$ is the photon energy and qV is the energy of the injected carriers based on the effective applied voltage. Assuming that the CNT–CNT spacing is long enough for the quantum efficiency to saturate, the power efficiency

© 2020 Wiley-VCH GmbH

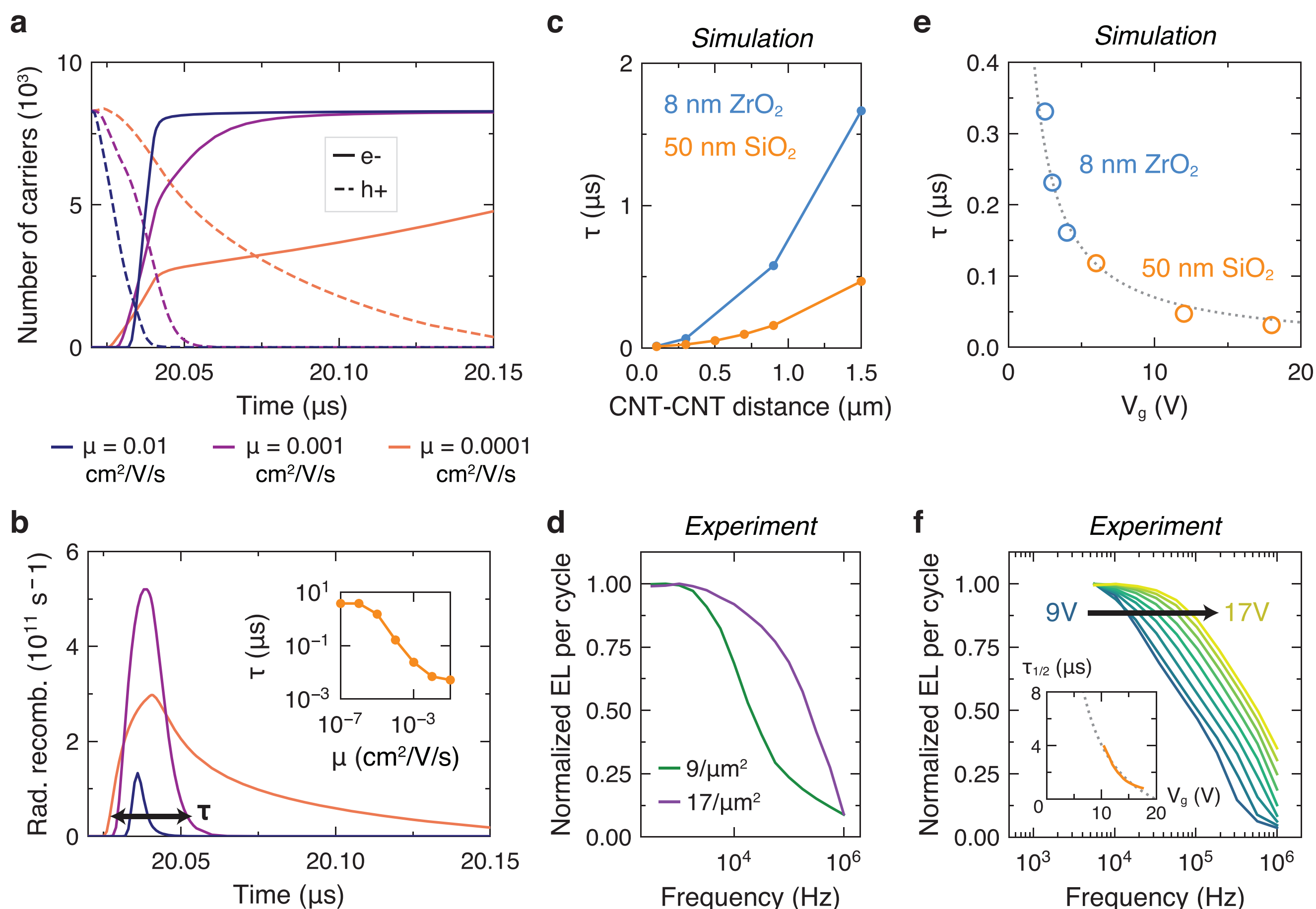

Figure 7. a,b) Simulated total number of carriers (a) and radiative recombination (b) versus time where an upward square wave transition from −12 V to +12 V is initiated at 20.02 µs. The solid and dashed lines in (a) represent electrons and holes. Simulations were performed for a 50 nm SiO_2 gate oxide device. The effective EL lifetime τ is calculated as the difference between the times when the EL rises and falls to 1% of its peak value. The inset in (b) shows τ as a function of carrier mobility in the emitter layer. c) Simulated EL lifetime as a function of CNT–CNT spacing. d) Experimentally measured EL intensity per square wave cycle as a function of square wave frequency for devices with CNT networks assembled for 5 min (≈9 CNT µm^{-2}) or 60 min (≈17 CNT µm^{-2}), where longer assembly times yield more dense CNT networks (shorter CNT–CNT distances). e) Simulated EL lifetime versus gate voltage for devices with different EOT. f) Experimentally measured EL intensity per square wave cycle as a function of square wave frequency for devices with gate voltages between 9 V (blue) and 17 V (yellow). The inset shows the time constant corresponding to the inverse of the frequency at which the normalized EL drops by half. The dotted lines in (e) and (f) represent inverse gate voltage scaling of the form $1/V_g$. Data were measured from 50 nm SiO_2 gate oxide devices with 9,10-diphenylanthracene (DPA) as the emitter.

tends to increase with the bandgap of the emissive material due to the higher energy of photons produced (Figure 6b). However, the turn-on voltage is also higher for larger bandgap materials, resulting in similar power efficiencies at the voltages required for similar emission intensities. Beyond the turn-on voltage, the maximum power efficiency decreases approximately inversely with applied gate voltage. The peak power efficiency for a thicker oxide device is lower than that of a thinner oxide device and occurs at a larger gate voltage because of the higher turn-on and operating voltages. Although the internal recombination efficiency can approach unity, the power efficiency lags the quantum efficiency in both simulation and experiment because each carrier type contributes to the electrical current when it enters and exits the material. Resistive losses in the large-area CNT network, which are neglected in the model, impose further reductions in power efficiency in the fabricated device.

Lastly, we investigated the temporal response of the device, which determines the maximum frequency or speed at which the gate voltage can be modulated while retaining linear frequency response. Even when external parasitic capacitances in the measured device are minimized, the lifetime of electroluminescence can still be limited by device characteristics such as carrier mobility. From the transient carrier density and EL profiles in **Figure 7**a,b, simulated using a square wave gate voltage, we observe that the number of holes in the emitter layer decreases and the number of electrons increases as the gate voltage switches from −12 to +12 V. This behavior is consistent with the mechanism in which downward band bending enables tunneling of electrons into the emitter layer as holes are extracted out, leading EL to occur for a finite period of time following the voltage transition. EL requires electron and hole populations to overlap in both space and time; as the mobility decreases, the time required for the slow holes to exit the semiconductor increases, and EL is longer-lived. The EL lifetime, calculated as the length of time in which the radiative recombination is at least 1% of its peak value, increases with

 © 2020 Wiley-VCH GmbH

decreasing carrier mobility but saturates at 10 µs (the length of a half-period of the 50 kHz applied square wave) for very low carrier mobility. Consequently, the emitter mobility should be increased if higher AC operating frequencies are desired, so that the device can reach steady-state conditions after each voltage transition. We performed device simulations using a higher frequency square wave gate voltage to confirm these trends (Figure S14, Supporting Information). With a 5 MHz square wave, the radiative recombination begins to fall off at a higher carrier mobility than for a 50 kHz square wave, as indicated by the similar levels of EL at $\mu \geq 10^{-3}$ cm^2 V^{-1} s^{-1} but lower EL at $\mu = 10^{-4}$ cm^2 V^{-1} s^{-1}. Band diagrams of the device operated at 50 kHz show a constant concentration of electrons accumulated in the emitter layer before a downward voltage transition, with almost no holes present. Flat energy bands along the lateral direction indicate that the applied gate voltage is dropped in the vertical direction across the oxide. On the other hand, the device operated at 5 MHz continues to show large quasi-Fermi level splitting in the emitter layer, meaning that a substantial population of holes is still present. At this frequency, the 0.1 µs long period of constant positive gate voltage is insufficient to allow the carrier populations and electrostatics to reach equilibrium.

A simple method to probe temporal device behavior is to measure the frequency-dependent EL intensity. The increase in EL lifetime with decreasing carrier mobility relates to the higher resistance imposed by the emissive material. Hence, increasing the CNT network density, or reducing the CNT-–CNT distance, should decrease the EL lifetime and increase the maximum frequency for which the EL intensity per voltage transition does not decrease. This behavior is confirmed in both simulation and experiment as shown in Figure 7c,d. The cut-off frequency in the experimentally measured data is around 100 kHz. This frequency corresponds to an EL lifetime of around 5 µs, which is higher than the simulated values. This suggests that parasitic *RC* delays in the fabricated microscale device structure, CNT network, and measurement setup may additionally contribute to prolonged EL responses, as well as differences in luminescent lifetimes of the experimentally measured and simulated emissive materials. The EL lifetime decreases with increasing gate voltage, at the expense of efficiency, as carriers in the emissive material are swept out more quickly under the influence of steeper potential profiles near the contact (Figure 7e). Experimental measurements show a similar trend in which the EL intensity per transition remains constant over a larger frequency range when the applied gate voltage is higher (Figure 7f). In the future, parasitic device resistances, which are currently largely dominated by the resistive CNT network used as the porous source contact, should be minimized to improve the operating frequency of the device and increase the time-averaged EL intensity.

In conclusion, we studied the performance of an AC electroluminescent device through numerical simulations and experiments, thereby guiding the rational design of high-performance AC electroluminescent devices for different applications. The model captures the essential physics of an AC electroluminescent device based on direct bipolar carrier injection and demonstrates that performance metrics are dictated by a combination of material properties, device structure, and operating parameters. In the ultimate limit of gate oxide scaling, EL can be generated at peak-to-peak gate voltages equal to the bandgap of the emitting material. Moreover, there are negligible differences in EL intensity and efficiency for materials with different energy level alignments with the source contact once the turn-on regime has been surpassed. The device thus renders electroluminescence spectroscopy a practical tool for studying and characterizing emissive materials with varying morphological, optical, and electronic properties in different environments. Since EL can be obtained from any material deposited on top of a pre-prepared device and does not require any specific material properties to occur, AC electroluminescent devices may serve as a promising solution for in situ metrology of unmodified materials and could have potential applications in a broad range of scientific fields in the future. Finally, the photon energy–bandgap scaling trends established from our model show that there are no fundamental limitations associated with generating EL from wide-bandgap materials, suggesting that AC injection may be a viable approach for developing LEDs in the deep-UV regime and beyond.

Experimental Section

Device Fabrication: 50 nm SiO_2/p++ Si substrates were subjected to O_2 plasma treatment for 1.5 min, immersed in poly-L-lysine solution for 5 min, then rinsed with deionized (DI) water. The substrate was subsequently immersed in 90% semiconducting CNT solution (NanoIntegris) for 30 min unless otherwise specified, then rinsed with DI water. Increasing the assembly time increased the density of the CNT network as reported previously.[40] Afterward, the substrate was annealed for 1 h in forming gas at 250 °C. Metal grid electrodes contacting the CNT network were patterned by photolithography and deposited by e-beam evaporation (0.5 nm Ti/25 nm Pd). CNTs outside the device area were patterned by photolithography and etched with O_2 plasma to prevent leakage. For devices with thin gate dielectric, 90 nm SiO_2/p++ Si substrates were patterned by photolithography and the exposed SiO_2 was etched completely away with 6:1 buffered oxide etch. Around 8 nm ZrO_2 was deposited at 180 °C by atomic layer deposition, followed by e-beam deposition of 2–3 nm SiO_x for adherence of CNT networks.[41] The remainder of device fabrication followed the process described earlier, except here metallic CNT networks were used as the source electrode to reduce the turn-on voltage. Metallic CNT networks were deposited by drop-casting 99% metallic CNT solution (NanoIntegris) on the substrate at 100 °C followed by a DI water rinse.

All emissive materials were purchased commercially from Sigma–Aldrich (unless otherwise noted) and prepared at room temperature under ambient conditions. Visible-wavelength QD emitter layers were prepared by drop-casting a 1 mg mL^{-1} solution of CdSSe/ZnS alloyed quantum dots in toluene on the device and letting the solution dry at room temperature. In this work, red and green QDs corresponded to 630 and 520 nm wavelength quantum dots, respectively. CdSeTe/ZnS quantum dots (NanoOptical Materials) were first washed (by adding 0.1 mL of the 5 mg mL^{-1} QD solution to 1.5 mL ethanol, centrifuging at 8800 rpm for 5 min, then decanting the clear supernatant) before redispersing in 0.2 mL toluene. The resulting solution was drop-cast on the device and left to dry at room temperature. To remove extra ligands, devices with CdSSe/ZnS or CdSeTe/ZnS QDs were immersed in acetone for 1 min, 1 wt% acetic acid in acetone for 5 min, and then acetone again for 1 min. PbS quantum dots (NNCrystal) were washed and redispersed in the same manner as the CdSeTe/ZnS QDs, then drop-cast on the device and left to dry at room temperature. The film was not washed afterward due to its tendency to delaminate when immersed in solution. $Ru(bpy)_3(PF_6)_2$ was deposited by drop-casting a 20 mg mL^{-1} solution of $Ru(bpy)_3(PF_6)_2$ in acetonitrile on the device and letting it dry on a

© 2020 Wiley-VCH GmbH

hotplate at 70 °C in air. 9,10-diphenylanthracene (DPA) was deposited by drop-casting a 10 mg mL^{-1} solution of DPA in toluene on the device and letting it dry at room temperature. For all drop-cast emitter materials, around 5 µL of solution was dispensed on chips of around 0.25 cm^2 in size. Poly(9,9-dioctylfluorene) (PFO) was measured by spin-coating a 5 mg mL^{-1} solution of PFO in toluene on the device at 6000 rpm.

Device Characterization: AC voltage was applied using an arbitrary waveform generator (Agilent 33522A) and a voltage amplifier for voltages beyond 10 V. Optical measurements were performed using a custom-built micro-PL instrument in which EL was dispersed by a spectrometer and detected with a charge-coupled device (CCD) (Andor iDus BEX2-DD). Emission power was measured with a power meter (Thorlabs PM100D with S120C sensor) and cross-calibrated with CCD counts. Electrical measurements were performed with a current amplifier (Stanford Research Systems SR570) and an oscilloscope. Devices were measured in vacuum (≈10 mTorr). The experimental IQE was determined by dividing the number of emitted photons (estimated from the EL power and emission spectrum) by the time-averaged number of injected electron–hole pairs (estimated by integrating the electrical current; refer to Figure S10 in the Supporting Information).

Device Simulation: In order to capture the basic physics of the device, 2D simulations of the device cross section were performed using Sentaurus TCAD (Synopsys) following a previously described approach.[21] The modeled device consisted of a layer of semiconducting material between two 1.4 nm tall edge contacts representing CNT source contacts. The underlying gate oxide layer (50 nm SiO_2 with $\varepsilon = 3.9$ unless otherwise stated) was contacted by a bottom gate electrode. For devices with a high-κ gate dielectric, the oxide dielectric constant was $\varepsilon = 22$. Unless otherwise specified, material parameters used for the semiconducting layer were E_g (bandgap) = 2 eV, ε (relative permittivity) = 3.5, μ_n (electron mobility) = μ_p (hole mobility) = 0.001 cm^2 V^{-1} s^{-1}, m_e* (electron effective mass) = m_h* (hole effective mass) = m_0 with CNT–CNT spacing L = 300 nm. These parameters were similar to those used in numerical simulations of optoelectronic devices with similar material systems.[42–44] Contact work functions were set to be midgap relative to the emitter bandgap in order to produce ambipolar behavior (i.e., symmetric results for upward and downward voltage transitions). For simplicity, a free carrier model with purely radiative recombination was assumed. A nonlocal tunneling model for electrons and holes at the source contact–semiconductor interface was applied. The total amount of radiative recombination was calculated by integrating the volume density of the radiative recombination rate over the volume of the emitter layer over one period of a 50 kHz square wave voltage applied between the gate and source contacts. The slew time (rise as well as fall time) of the square wave gate voltage was 20 ns.

Supporting Information

Supporting Information is available from the Wiley Online Library or from the author.

Acknowledgements

Device design and characterization were supported by the NSF Center for Energy Efficient Electronics Science. Material characterization, including luminescence studies, was supported by the Electronic Materials Program, funded by the Director, Office of Science, Office of Basic Energy Sciences, Materials Sciences and Engineering Division of the US Department of Energy under Contract No. DE-AC02-05Ch11231. Device modeling was supported by Samsung. V.W. is supported by an NSF Graduate Research Fellowship under Grant No. DGE-1752814.

Conflict of Interest

The authors declare no conflict of interest.

Keywords

alternating current, carbon nanotubes, electroluminescence, light-emitting devices

Received: August 19, 2020
Revised: October 29, 2020
Published online:

[1] S. Nakamura, T. Mukai, M. Senoh, *Appl. Phys. Lett.* **1994**, *64*, 1687.
[2] C. P. Kuo, R. M. Fletcher, T. D. Osentowski, M. C. Lardizabal, M. G. Craford, V. M. Robbins, *Appl. Phys. Lett.* **1990**, *57*, 2937.
[3] Y. H. Won, O. Cho, T. Kim, D. Y. Chung, T. Kim, H. Chung, H. Jang, J. Lee, D. Kim, E. Jang, *Nature* **2019**, *575*, 634.
[4] X. Dai, Z. Zhang, Y. Jin, Y. Niu, H. Cao, X. Liang, L. Chen, J. Wang, X. Peng, *Nature* **2014**, *515*, 96.
[5] Y. Liu, C. Li, Z. Ren, S. Yan, M. R. Bryce, *Nat. Rev. Mater.* **2018**, *3*, 18020.
[6] H. Kaji, H. Suzuki, T. Fukushima, K. Shizu, K. Suzuki, S. Kubo, T. Komino, H. Oiwa, F. Suzuki, A. Wakamiya, Y. Murata, C. Adachi, *Nat. Commun.* **2015**, *6*, 8476.
[7] Y. Pan, Y. Xia, H. Zhang, J. Qiu, Y. Zheng, Y. Chen, W. Huang, *Adv. Mater.* **2017**, *29*, 1701441.
[8] A. G. Fischer, *J. Electrochem. Soc.* **1963**, *110*, 733.
[9] T. Tsutsui, S. B. Lee, K. Fujita, *Appl. Phys. Lett.* **2004**, *85*, 2382.
[10] Y. Chen, Y. Xia, G. M. Smith, H. Sun, D. Yang, D. Ma, Y. Li, W. Huang, D. L. Carroll, *Adv. Funct. Mater.* **2014**, *24*, 2677.
[11] J. Sung, Y. S. Choi, S. J. Kang, S. H. Cho, T. W. Lee, C. Park, *Nano Lett.* **2011**, *11*, 966.
[12] S. H. Cho, J. Sung, I. Hwang, R. H. Kim, Y. S. Choi, S. S. Jo, T. W. Lee, C. Park, *Adv. Mater.* **2012**, *24*, 4540.
[13] D. H. Lien, M. Amani, S. B. Desai, G. H. Ahn, K. Han, J. H. He, J. W. Ager, M. C. Wu, A. Javey, *Nat. Commun.* **2018**, *9*, 1229.
[14] J. Cho, M. Amani, D. Lien, H. Kim, M. Yeh, V. Wang, C. Tan, A. Javey, *Adv. Funct. Mater.* **2020**, *30*, 1907941.
[15] X. Liu, D. Yu, C. Huo, X. Song, Y. Gao, S. Zhang, H. Zeng, *Adv. Opt. Mater.* **2018**, *6*, 1800206.
[16] F. Maddalena, X. Y. Chin, D. Cortecchia, A. Bruno, C. Soci, *ACS Appl. Mater. Interfaces* **2018**, *10*, 37316.
[17] T. Yamao, Y. Shimizu, K. Terasaki, S. Hotta, *Adv. Mater.* **2008**, *20*, 4109.
[18] J. Simon, J.-J. André, *Molecular Semiconductors*, Springer, Berlin, Germany **1985**.
[19] Y. Shirota, H. Kageyama, *Chem. Rev.* **2007**, *107*, 953.
[20] E. S. Snow, J. P. Novak, P. M. Campbell, D. Park, *Appl. Phys. Lett.* **2003**, *82*, 2145.
[21] Y. Zhao, V. Wang, D. H. Lien, A. Javey, *Nat. Electron.* **2020**, *3*, 612.
[22] R. F. Pierret, in *Semiconductor Device Fundamentals* (Ed: K. Harutunian), Addison-Wesley, New York **1996**.
[23] C. D. J. Blades, A. B. Walker, *Synth. Met.* **2000**, *111*, 335.
[24] V. Wood, J. E. Halpert, M. J. Panzer, M. G. Bawendi, V. Bulović, *Nano Lett.* **2009**, *9*, 2367.
[25] V. Wood, M. J. Panzer, D. Bozyigit, Y. Shirasaki, I. Rousseau, S. Geyer, M. G. Bawendi, V. Bulović, *Nano Lett.* **2011**, *11*, 2927.
[26] J. Robertson, *EPJ Appl. Phys.* **2004**, *28*, 265.
[27] A. Perumal, B. Lüssem, K. Leo, *Appl. Phys. Lett.* **2012**, *100*, 103307.
[28] B. K. Crone, P. S. Davids, I. H. Campbell, D. L. Smith, *J. Appl. Phys.* **1998**, *84*, 833.
[29] C. G. Shuttle, R. Hamilton, J. Nelson, B. C. O'Regan, J. R. Durrant, *Adv. Funct. Mater.* **2010**, *20*, 698.
[30] Z. Deng, S. T. Lee, D. P. Webb, Y. C. Chan, W. A. Gambling, *Synth. Met.* **1999**, *107*, 107.

© 2020 Wiley-VCH GmbH

[31] J. Liu, H. Zhang, H. Dong, L. Meng, L. Jiang, L. Jiang, Y. Wang, J. Yu, Y. Sun, W. Hu, A. J. Heeger, *Nat. Commun.* **2015**, *6*, 10032.
[32] J. Li, K. Zhou, J. Liu, Y. Zhen, L. Liu, J. Zhang, H. Dong, X. Zhang, L. Jiang, W. Hu, *J. Am. Chem. Soc.* **2017**, *139*, 17261.
[33] D. J. Harkin, K. Broch, M. Schreck, H. Ceymann, A. Stoy, C.-K. Yong, M. Nikolka, I. McCulloch, N. Stingelin, C. Lambert, H. Sirringhaus, *Adv. Mater.* **2016**, *28*, 6378.
[34] G. G. Malliaras, J. C. Scott, *J. Appl. Phys.* **1998**, *83*, 5399.
[35] T. Matsushima, F. Bencheikh, T. Komino, M. R. Leyden, A. S. D. Sandanayaka, C. Qin, C. Adachi, *Nature* **2019**, *572*, 502.
[36] N. K. Patel, S. Ciná, J. H. Burroughes, *IEEE J. Sel. Top. Quantum Electron.* **2002**, *8*, 346.
[37] S. Bernhard, J. A. Barron, P. L. Houston, H. D. Abruña, J. L. Ruglovksy, X. Gao, G. G. Malliaras, *J. Am. Chem. Soc.* **2002**, *124*, 13624.
[38] W. H. Elfring, G. A. Crosby, *J. Am. Chem. Soc.* **1981**, *103*, 2683.
[39] G. E. Jabbour, J. F. Wang, N. Peyghambarian, *Appl. Phys. Lett.* **2002**, *80*, 2026.
[40] T. Takahashi, Z. Yu, K. Chen, D. Kiriya, C. Wang, K. Takei, H. Shiraki, T. Chen, B. Ma, A. Javey, *Nano Lett.* **2013**, *13*, 5425.
[41] C. Wang, J. C. Chien, K. Takei, T. Takahashi, J. Nah, A. M. Niknejad, A. Javey, *Nano Lett.* **2012**, *12*, 1527.
[42] F. F. Stelzl, U. Würfel, *Phys. Rev. B: Condens. Matter Mater. Phys.* **2012**, *86*, 075315.
[43] P. Kaienburg, U. Rau, T. Kirchartz, *Phys. Rev. Appl.* **2016**, *6*, 024001.
[44] T. Kirchartz, J. Nelson, U. Rau, *Phys. Rev. Appl.* **2016**, *5*, 054003.

© 2020 Wiley-VCH GmbH